Optica Applicata, Vol. XLIII, No. 3, 2013
DOI: 10.5277/oa130319

Influence of surface plasmon wave interference on near-field imaging on metal nanostructures with apertured probe

YING YANG, ZHIJUN SUN*

Department of Physics, Xiamen University, Xiamen, Fujian 361005, China

*Corresponding author: sunzj@xmu.edu.cn

We numerically studied artifact issues on near-field imaging of field intensity on metal nanostructures (isolated ridges and slits in a continuous film) with an apertured probe. It is shown for the latter case that the interaction between neighboring slits via propagating surface plasmon waves (*e.g.*, surface plasmon wave interferences) makes the probe-imaged field intensity highly conditional in reflection of the unperturbed field. As surface plasmon behaviors and probe imaging processes are polarization-sensitive and the field components are correlated, a model analysis of the partial field components elucidates their relations, which can help to derive the unperturbed near-field image from the probed one.

Keywords: near-field, surface plasmon, metal, nanostructure.

1. Introduction

Near-field (NF) microscopy makes optical imaging of subwavelength objects possible, and nowadays it is also used to obtain near-field information in various light-matter interactions [1–3]. With the emergence of plasmonics in recent years, the technique has been applied to image the surface plasmon (SP) waves or near-field distributions of the field intensity on metal nanostructures [4–13]. SPs are harmonically oscillating polaritons of collective charges (free electrons) coupled with electromagnetic (EM) waves at metal surfaces; fundamentally their properties can be derived from each other. Therefore, SP waves can be "observed" by either monitoring oscillations of the electrons [14–16] or imaging field distributions of the EM waves. In near-field imaging of field distributions, the presence of the probe usually modifies the local field, especially when the scanned surface is highly structured with sharp morphologies. As a result, the detected signal from the NF probe may not directly reflect the profile of the structures or unperturbed field distributions [17]. But usually, the real structures or field profiles can be reconstructed using deconvolution methods from the probed ones [18], provided that the structure units are isolated and they do not have strong

inter-correlations in optical interactions so that the results of each unit can be linearly superposed as contributions to the final observations. The approach is well used in imaging near-field profiles of dielectric-type structures. But for metallic structures, due to strong optical interactions in the near-field region and diversified conditional behaviors of SPs, the unperturbed field profiles cannot be usually obtained this way, though there are reports based on direct imaging of the SP fields with NF probing as mentioned above. Currently, there is a lack of such work to clarify the issues. In this paper, we do investigations on some basic metal structures, nanoslit(s), to show their relations that may help to derive the unperturbed field from the probed one using apertured probes.

In the following, we will first show briefly the probed field profiles of isolated nano-ridges and compare them with those scanned without the probe as a background (Section 2). Section 3 will be our emphasis to give a detailed analysis of near-field imaging of the field profiles on a metal film with slits upon optical transmission. Finally, we summarize the conclusions in Section 4. In the work, the 3-dimensional finite-difference time-domain (FDTD) method is used for numerical simulations. The apertured probe in simulations has a tapered (tapering angle of 45°) dielectric core of index 1.5 coated with a 100-nm-thick silver layer, and the diameter of the aperture is 80 nm, similar to those of commercial ones. The scanning is performed at a constant height h of 60 nm in the simulations, and intensity of the field coupled into the probe is recorded with a monitor set inside the probe. The probed results are compared with those obtained without the probe, in which there is only a monitor of size $\Delta x = \Delta z = = 30$ nm and $\Delta y = 10$ nm, scanning at an equal constant height of 60 nm above the structure to record the field intensity. The structures in study are assumed to be on a dielectric substrate of index 1.5, and the input light is normally incident from the substrate side in transverse-magnetic (TM) polarizations.

2. Near-field imaging on isolated nano-ridges

Below we show the field intensity on isolated metallic and dielectric ridges scanned with or without the probe. Figure 1**a** is a schematic illustration of the setup in simulations. The ridges are either metal of Ag or dielectric with an index of 1.5 (*e.g.*, SiO_2) with cross-section dimensions of $a = b = 50$ nm. Vacuum wavelength of the incidence light is assumed to be $\lambda = 600$ nm. The scanned field intensities on a single or two dielectric ridges with a separation of $s = 300$ nm are shown in Figs. 1**b** and 1**c**, and those for metal ridges in Figs. 1**d** and 1**e**. Noted that shown in the plots are relative intensity values obtained by normalizing the original data with the maximum value in each scan.

The results in Figs. 1**b** and 1**d** show that, for a single dielectric or metal ridge, the profile of the unperturbed field intensity has a dip just above the ridges and two peaks on both sides; it is not shown here that, as the scanning height is smaller, the dip and peaks will have a larger contrast. While for the probe imaged field intensity profiles, there is only one peak corresponding to the ridges, and contrasts of the profiles

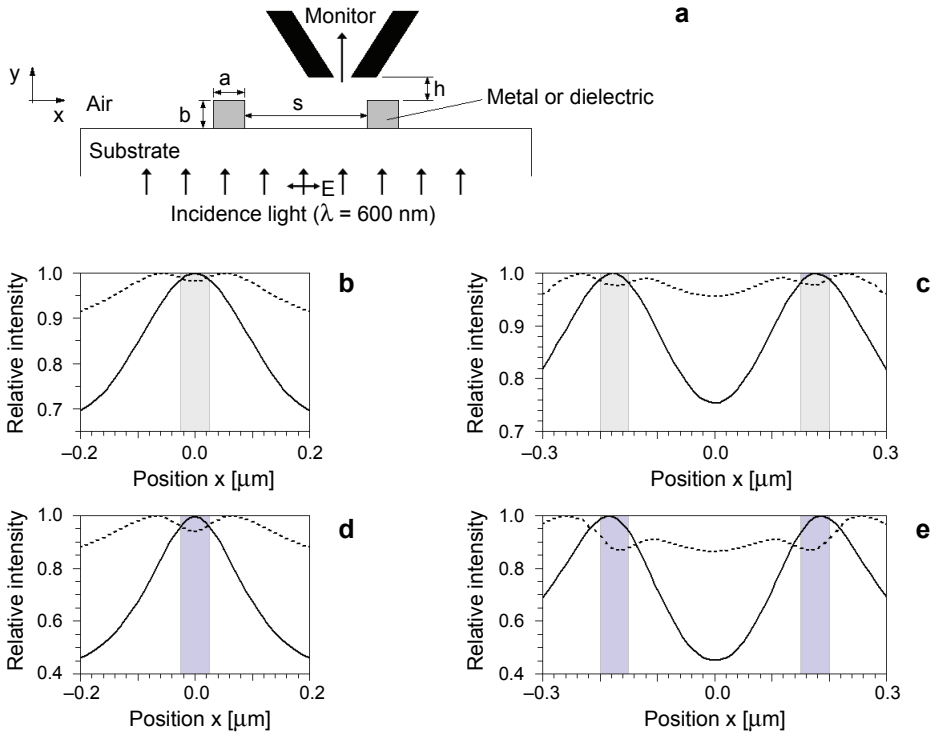

Fig. 1. Schematic illustration of near-field probe imaging on isolated ridges (**a**). Constant-height-scanning field intensity on isolated ridges recorded with (solid lines) or without (dashed lines) the probe (**b**–**e**); **b**, **c** – for dielectric ridges, and **d**, **e** – for metal ridges. In all, dimensions of the ridges are $a = b = 50$ nm, and $s = 300$ nm for two ridges. The shaded regions correspond to positions of the ridges.

are much larger than those of the unperturbed one. This suggests a strong interaction between the object and the probe. It is more important to find in Figs. 1**c** and 1**e** that field intensity profiles of the two-ridge structures are just a superposition of the profiles of individual ones, for both the dielectric and metal ridge structures and for both the unperturbed and probe imaged intensity profiles. This provides us with a general way to qualitatively derive the unperturbed field intensity profiles (or images) from the probed one using the corresponding relation obtained for a single ridge as a reference, ignoring the contrast of the profiles. Besides, the subwavelength structures can also be imaged this way by using the reconstruction method mentioned previously. We may not need to know the specific probe-object interaction processes here, provided that optical interactions with each individual structure unit do not strongly affect those of the others.

3. Near-field imaging on slits in a metal film

We performed similar simulations for the structures of narrow slit(s) in a dielectric or metal film (complementary structures of isolated ridges), as shown in Fig. 2. The simu-

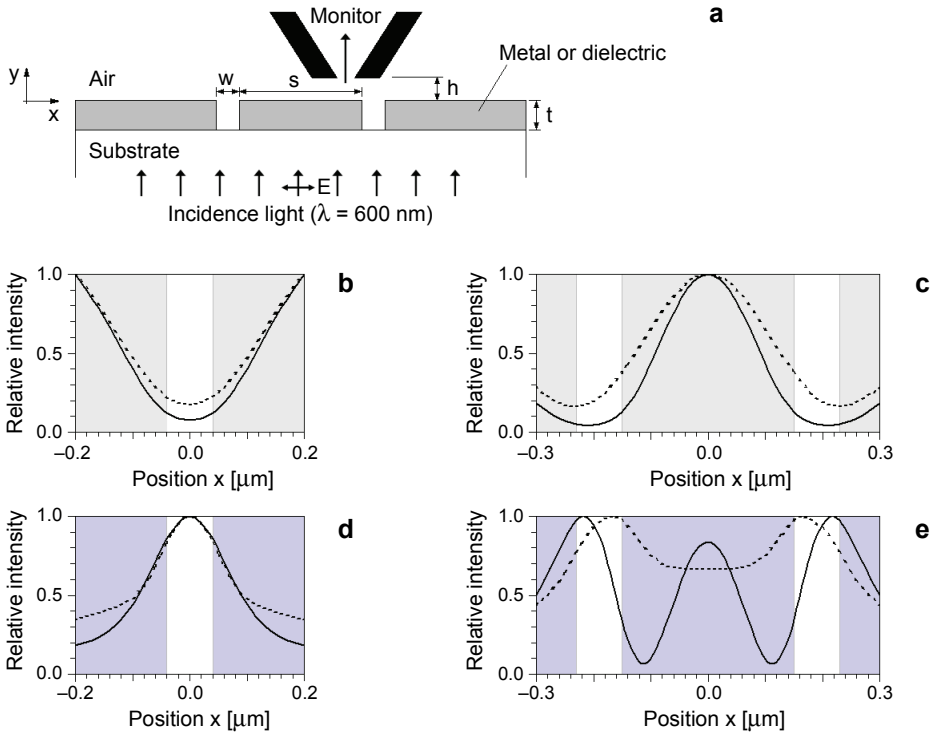

Fig. 2. Schematic illustration of near-field probe imaging on a metal or dielectric film with slit(s) (**a**). Constant-height-scanning field intensity on a metal film with slit(s) recorded with (solid lines) or without (dashed lines) the probe (**b**–**e**); **b**, **c** – for slits in a dielectric film, and **d**, **e** – for slits in a metal film. In all, dimensions of the slits are w = 80 nm, t = 200 nm, and s = 300 nm for two slits. The shaded regions correspond to the metal or dielectric regions.

lation conditions are same as those in Section 2, except for differences of the structures (Fig. 2**a**). Here, thicknesses of the dielectric (index 1.5) or metal (Ag) films are t = 200 nm, widths of the slits are w = 80 nm, and separations of the two slits in Figs. 2**c** and 2**e** are s = 300 nm. It is shown in Figs. 2**b** and 2**d** that, for a single slit in a dielectric or metal film, the probe imaged intensity profiles roughly reflect the unperturbed ones, except at the positions away from the slit in the metal case (Fig. 2**d**). It is shown in Fig. 2**c** that, for the structures of two slits in a dielectric film, the probed intensity profile can also be considered as a superposition of those of the individual slits, similar to that of the isolated ridge structures in Fig. 1. But for the metal case in Fig. 2**e**, a peak clearly appears for the probed one in the region between the two slits, which cannot be considered as a result of superposition.

From the simulation results above, it is generally observed that the unperturbed field intensity profiles and their subwavelength structures can both be derived roughly from their probe imaged field intensity profiles, except for the metallic narrow slit structures. The exception for the slit structures is related to support the propagating SP waves at the flat metal surfaces. The interference of propagating SP waves excited

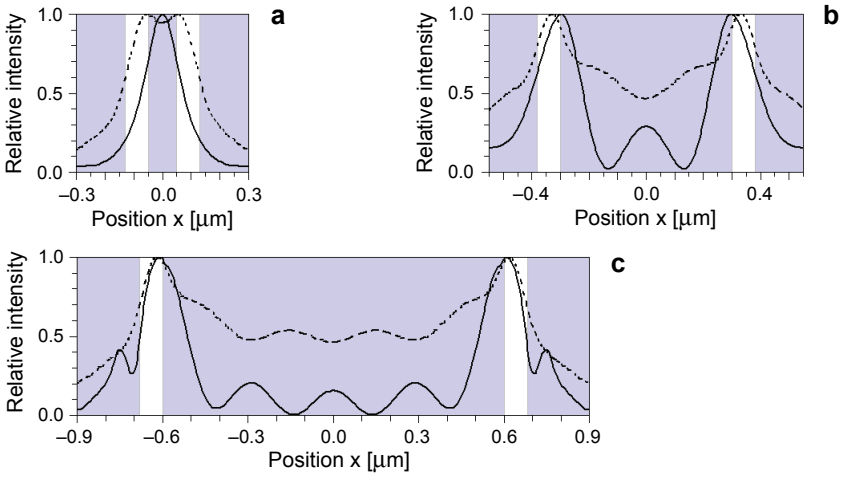

Fig. 3. Constant-height-scanning field intensity on a metal film with two slits of different interspacings recorded with (solid lines) or without (dashed lines) the probe; $s = 100$ nm (**a**), $s = 600$ nm (**b**) and $s = 1200$ nm (**c**). All other dimensions are same as those in Fig. 2**e**. The shaded regions correspond to the metal surface.

at the exits of neighboring slits changes the near-field intensity distributions on top of the interval metal surface region. Meanwhile, the interaction between the probe and the structure becomes also different; it is shown later that the probe fundamentally modifies the propagating SP wave modes instead of simply "picking up" the local field with its aperture.

Figure 3 shows simulated distributions of the field intensity on the structures with two narrow slits ($w = 80$ nm) of smaller and even larger interspacings ($s = 100$, 600, 1200 nm), in addition to the results for $s = 300$ nm in Fig. 2**e**. It is observed, more clearly in Fig. 3**c**, that symmetric distribution of the scanned field intensity has a maximum at the middle position ($x = 0$) between the two slits for the probed results, but has a minimum for the unperturbed ones; and fluctuations of their field intensity distributions are roughly in opposite phase. It is also noticed that a strong field intensity maximum appears not right above the center of each slit, but slightly shifted inwards for both scanning results. As a result, for very small interspacings, *e.g.*, $s = 100$ nm in Fig. 3**a**, the probe scanned field intensity will show one maximum right above the ridge between the slits instead of the slits themselves. The results suggest that the probe imaged distributions of field intensity on such structured metal surfaces do not directly reflect the unperturbed real field distributions, but they have certain relations. In the following, a model is proposed to clarify their relations and explain the simulation results.

As schematically illustrated in Fig. 4**a**, upon transmission of TM-polarized incidence light through the narrow slits in a metal film, the transmitted power can be considered to be decoupled into two components: the in-plane propagating SP waves and the cylindrically emanating free-space (CF) light waves, whose wavevectors are

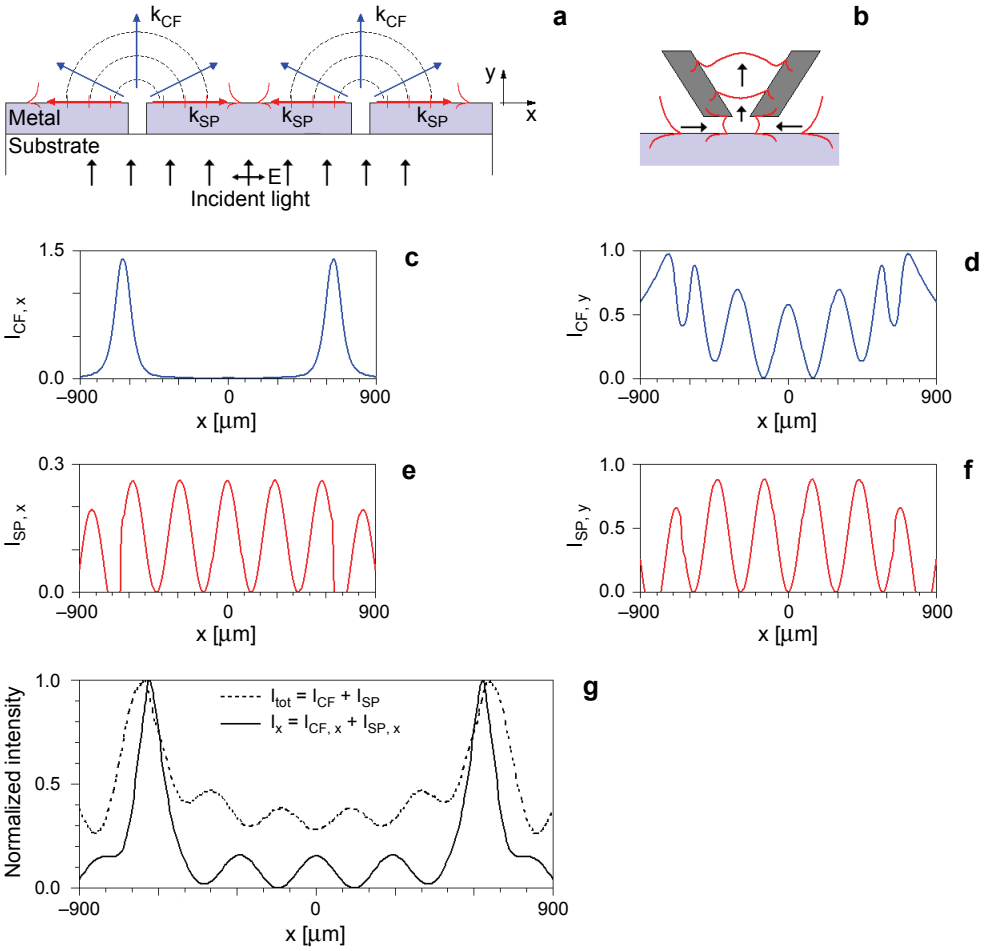

Fig. 4. Schematic illustration of the generated in-plane SP waves and cylindrical free-space wave emitted from the slit antenna (**a**). Schematic illustration of coupling in-plane SP waves at the metal/air interface into the probe (**b**). Modeled intensity distribution of different polarization components of the cylindrical free-space wave and SP waves under interferences of waves generated from two slits (s = 1200 nm) at a constant height of h = 60 nm (**c**–**f**). Modeled distributions of the total field intensity (solid line) and x-polarization field intensity (dashed line) of two types of wave components (**g**).

denoted with k_{SP} and k_{CF} in magnitude, respectively. Thus field components of the two waves are $\{H_z^{CF}; H_\theta^{CF}\}$ for the CF waves in a polar coordinate, and $\{H_z^{SP}; E_x^{SP}, E_y^{SP}\}$ for the SP waves in the top air side of the Ag/air interface.

Firstly, consider only one slit and define middle point of its exit as the coordinate origin, the electric fields of the emitted waves can be approximately written in the following forms:

$$E_\theta^{CF} = \hat{e}_\theta \cdot E_0^{CF} \sqrt{\frac{C_1}{r}} \exp\left[i(k_{CF} r + \phi_1)\right] \tag{1}$$

$$E_x^{\mathrm{SP}} = \hat{e}_x \cdot E_{x0}^{\mathrm{SP}} \exp\left[i(k_{\mathrm{SP}}x + \phi_2)\right] \exp(i\gamma_{\mathrm{SP}}y) \tag{2}$$

$$E_y^{\mathrm{SP}} = \hat{e}_y \cdot E_{y0}^{\mathrm{SP}} \exp\left[i(k_{\mathrm{SP}}x + \phi_3)\right] \exp(i\gamma_{\mathrm{SP}}y) \tag{3}$$

Here E_0^{CF}, E_{x0}^{SP}, E_{y0}^{SP} and are amplitudes of the fields, $k_{\mathrm{CF}} = k_0 = 2\pi/\lambda$, $k_{\mathrm{SP}} = (2\pi/\lambda)\sqrt{\varepsilon_m/(1+\varepsilon_m)}$, $\gamma_{\mathrm{SP}} = \sqrt{k_0^2 - k_{\mathrm{SP}}^2}$, ε_m is the permittivity of the metal (Ag), $r = \sqrt{x^2 + y^2}$, C_1 is a constant quantity dependent on the intensity of the CF waves at the position of a slit exit, and ϕ_1, ϕ_2 and ϕ_3 are initial phases of the wave fields. According to fundamentals of the SP wave, amplitudes of longitudinal and transverse field components of the SP waves have the relation:

$$\frac{E_y^{\mathrm{SP}}}{E_x^{\mathrm{SP}}} = \frac{k_{\mathrm{SP}}}{\gamma_{\mathrm{SP}}} = R\exp(i\varphi) \tag{4}$$

where R is real and $\varphi = \phi_3 - \phi_2$. *E.g.*, for SP waves at an air/Ag interface and $\lambda = 600$ nm, $R = 3.56$, $\varphi = 87.8°$. Meanwhile, intensity contributions of the power due to y- and x-components of the SP fields also have the ratio:

$$\frac{I_{\mathrm{SP}}^{(y)}}{I_{\mathrm{SP}}^{(x)}} = \frac{\langle |S_x| \rangle}{\langle |S_y| \rangle} = \frac{\langle \left| E_y^{\mathrm{SP}} \cdot H_z^{\mathrm{SP}} \right| \rangle}{\langle \left| E_x^{\mathrm{SP}} \cdot H_z^{\mathrm{SP}} \right| \rangle} = \left| \frac{k_{\mathrm{SP}}}{\gamma_{\mathrm{SP}}} \right| = R \tag{5}$$

Thus, distribution of the field intensity above the metal surface with a single slit can be expressed as $I_{1\text{-slit}}(x, y) = I_{\mathrm{CF}}(r) + I_{\mathrm{SP}}(x, y)$, where $I_{\mathrm{CF}} = C_1 \left| E_0^{\mathrm{CF}} \right|^2 / r$ and $I_{\mathrm{SP}} = I_{\mathrm{SP}}^{(x)} + I_{\mathrm{SP}}^{(y)} = C_2(1+R)\left| E_x^{\mathrm{SP}} \right|^2$, C_1 and C_2 are constants. Here we also introduce a parameter of ratio $\xi = \left| E_x^{\mathrm{SP}} \right|^2 / \left| E_0^{\mathrm{CF}} \right|^2$, which characterizes distribution of the transmitted power on the CF and SP wave components.

For the two-slit case, there are interferences of the same types of wave components emanated from each slit. According to Maxwell's equations, $E_x^{\mathrm{SP}} \sim \partial H_z^{\mathrm{SP}}/\partial y$ and $E_y^{\mathrm{SP}} \sim \partial H_z^{\mathrm{SP}}/\partial x$, SP waves emitted from the slit-exits propagating in opposite x-directions at the metal surface are symmetrically in phase for the E_x^{SP} field, and anti-symmetrically in opposite phase for the E_y^{SP} field. As a result of interference of SP wave fields from two slits, the E_x^{SP} field has a maximum while the E_y^{SP} field has a minimum at the middle position between the two slits at the metal surface. As we define $x = 0$ at the middle line in this case, and $\left| E_0^{\mathrm{CF}} \right|^2 = I_0$, the field intensity above the metal surface with two identical slits can be written as follows based on the conditions above:

$$I_{2\text{-slit}}(x, y) = I_{\mathrm{CF}} + I_{\mathrm{SP}} = (I_{\mathrm{CF},\,x} + I_{\mathrm{CF},\,y}) + (I_{\mathrm{SP},\,x} + I_{\mathrm{SP},\,y}) \tag{6}$$

where

$$I_{\mathrm{CF},x} = \frac{I_0}{r}\cos^2(\theta) \tag{7}$$

$$I_{\mathrm{CF},y} = \frac{I_0}{r}\sin^2(\theta) \tag{8}$$

$$I_{\mathrm{SP},x} = 2\xi I_0 \exp(-k_{\mathrm{SP2}}s)\left[\cosh(2k_{\mathrm{SP2}}x) + \cos(2k_{\mathrm{SP1}}x)\right]\exp(-2\gamma_{\mathrm{SP2}}y) \tag{9}$$

$$I_{\mathrm{SP},y} = 2\xi R I_0 \exp(-k_{\mathrm{SP2}}s)\left[\cosh(2k_{\mathrm{SP2}}x) - \cos(2k_{\mathrm{SP1}}x)\right]\exp(-2\gamma_{\mathrm{SP2}}y) \tag{10}$$

In derivation of the equations, it is assumed that $|k_{\mathrm{SP1}}| \gg |k_{\mathrm{SP2}}|$, $|\gamma_{\mathrm{SP1}}| \ll |\gamma_{\mathrm{SP2}}|$ for $k_{\mathrm{SP}} = k_{\mathrm{SP1}} + ik_{\mathrm{SP2}}$ and $\gamma = \gamma_1 + i\gamma_2$. Let $I_0 = 100$ for $C_1 = 1$ and $r(x, y)$ in nanometer, and $\xi = 4.5\times10^{-4}$; we calculated the components of field intensity on a two-slit metal surface with $w = 80$ nm and $s = 1200$ nm at $\lambda = 600$ nm, the results are shown in Figs. 4**c**–4**f**. Further, the total field intensity ($I_{\mathrm{total}} = I_{\mathrm{CF}} + I_{\mathrm{SP}}$) and combination of the field intensity due to x-polarization fields ($I_x = I_{\mathrm{CF},x} + I_{\mathrm{SP},x}$) are calculated and plotted in Fig. 4**g** with their normalized values. It is indicated that distributions of the total and x-polarization field intensities are closely similar to those of unperturbed and probe imaged field intensities in Fig. 3**c** obtained with numerical simulations, though the effect of the probe is not considered at all for the modeled results in Fig. 4.

Figure 4**b** schematically illustrates coupling of the near-field SP waves into the apertured probe upon its presence. In the region between the two slits above the metal surface, the SP waves propagating towards the probe in both directions will firstly couple into another SP mode in the gap between the metal coated on the probe and the metal surface of the sample [19], then further couple into the probe core region. In spite of complex SP interactions involved in the coupling processes, as the probe is rotarily symmetric, interference of SP waves coupled into the probe will be same as that without the probe at the position of the probe aperture, due to equal SP wave path and coupling efficiencies at the junctions for mode conversion in both directions. Of course, the absolute value of the probe-detected SP field intensity will be smaller, but this is not a matter of concern in a normalized intensity profile. It is also known that detection with the near-field probe is more sensitive to the component of electric field parallel to the scanning surface, thus only contributions from x-polarization field (I_x) will be reflected in the probed intensity profile. Additionally, in $I_x = I_{\mathrm{CF},x} + I_{\mathrm{SP},x}$, the component of $I_{\mathrm{CF},x}$ dominates in the regions just above the slits and the $I_{\mathrm{SP},x}$ in interval metal surfaces. The situation is the same for the probed field intensity. As such, once we have the probed field intensity profile, we can get the unperturbed one by simply inversing the maxima and minima of interference fringes in the metal surface region while keep those in the slit regions; here a background value of the intensity profile is usually not a concern.

4. Near-field imaging on periodic nanoslits in a metal film and effects of SP resonances

In the analysis above, the interference of SP waves at the metal surface is not designed to be resonant. To see the effect of resonance conditions, we do investigations on a structure of periodic metallic nanoslit arrays, which has been widely studied in the field of plasmonics. The structure is same as that studied in Section 3, except for its periodicity. In Figure 5**a**, we show the simulated transmission spectrum of such a structure with 200-nm-thick metal film, 80-nm-wide slits and 400-nm period. It has been identified that the spectrum dips at $\lambda = 440$ and 650 nm are due to resonances of SP waves at the top (air/Ag) and bottom (substrate/Ag) interfaces, respectively, and

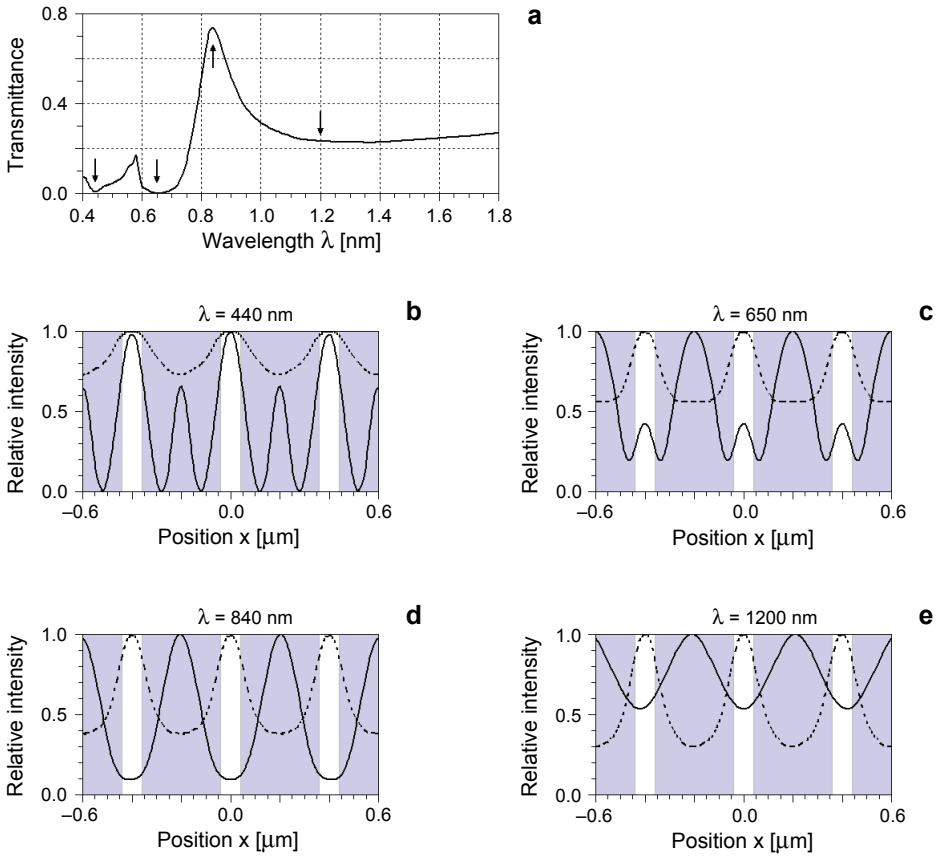

Fig. 5. Optical transmission spectrum of a periodic metal (Ag) slit array ($p = 400$ nm, $w = 80$ nm, $t = 200$ nm) (**a**). Constant-height-scanning field intensity on top of the slit array at different wavelengths of the incidence light recorded with (solid lines) or without (dashed lines) the probe; the shaded regions correspond to the metal surface (**b**–**e**).

the peak at $\lambda = 840$ nm is due to Fabry–Pérot-like resonance of gap SP waves in the slits [20]. Thus we simulated scanning of the field intensity on the period metal nanoslit array as before at the resonance wavelengths and $\lambda = 1200$ nm in the long--wavelength regime. The results are shown in Fig. 5**b**–5**d**. It is observed that, for the structure with subwavelength period, the unperturbed field intensity shows a maximum in the positions of slits and a valley in the regions above the metal surface at all wavelengths, no matter whether or not it is in a resonance condition. There is only a trend that contrasts of the field intensity profiles will be larger at longer wavelengths that are more off the resonance positions. For the probe imaged profiles, under the condition of SP resonance at the air/Ag surface in Fig. 5**b**, there is a distinct peak in each metal surface region, besides there is also a high peak above each slit. The corresponding relation between the probed and unperturbed field intensity profiles is same as that observed for the two-slit case. But as the wavelength increases, the peaks above the slits come to be relatively weaker and the peaks above the metal surface regions become stronger, *e.g.*, in Fig. 5**c**. At even longer wavelengths, there are only peaks above the metal surface regions, *e.g.*, in Figs. 5**d** and 5**e**. The probe scanned field intensity profiles are totally reversed in fluctuations compared to the unperturbed ones scanned without the probe, similar to the case in Fig. 3**a** for two slits with very small interspacing (relative to the wavelength). Thus, the probe scanned field intensity profiles are reflections of the field interference effects; SP resonances are not necessary to be particularly considered.

5. Conclusions

We simulated near-field imaging of the field intensity on metal and dielectric nanostructures of isolated ridges or nanoslits. It has been shown that the probe scanning of structures with slits in metal films is highly subject to the interference of SP waves at the metal surfaces, which emanate from each slit. Although distributions of the probe imaged field intensity are very different from those unperturbed, their correlations inform us to derive the unperturbed ones from the probed ones. *I.e.*, if the interspacings of slits, whether periodic or only a few, are in the subwavelength regime ($s < \lambda$), peaks and valleys in fluctuations of the probed scanned field intensity correspond respectively to the valleys in the metal surface regions and peaks at the slit regions of the unperturbed field intensity profiles; if the interspacings of slits are larger than the half-wavelength ($s > \lambda/2$), strong peaks of the probe scanned field intensity profiles locate at the position of slits, and fluctuations appear in the segments of metal surfaces whose peaks and valleys correspond to the valleys and peaks of the unperturbed field intensity distributions. The model analysis shows that the probe imaged field intensities are reflections of distributions of the electric fields parallel to the metal surfaces, and their relation to the total fields are discussed. It is finally mentioned that, although the study is mainly on apertures of slits in the metal, the conclusions may

also be informative to understand near-field probe scanning of other structured metal surfaces.

Acknowledgements – The research is partially supported by the NSFC (No. 61275063), Natural Science Foundation of Fujian Province of China (No. 2011J06002) and the Fundamental Research Funds for the Central Universities (No. 2012121009).

References

[1] KAWATA S., OHTSU M., IRIE M., [Eds.], *Nano-Optics*, Springer-Verlag, Berlin Heidelberg, 2002.

[2] HAYAZAWA N., INOUYE Y., SEKKAT Z., KAWATA S., *Near-field Raman imaging of organic molecules by an apertureless metallic probe scanning optical microscope*, Journal of Chemical Physics **117**(3), 2002, pp. 1296–1301.

[3] ZHEYU FANG, CHENFANG LIN, RENMIN MA, SHAN HUANG, XING ZHU, *Planar plasmonic focusing and optical transport using CdS nanoribbon*, ACS Nano **4**(1), 2010, pp. 75–82.

[4] BOZHEVOLNYI S.I., VOHNSEN B., SMOLYANINOV I.I., ZAYATS A.V., *Direct observation of surface polariton localization caused by surface roughness*, Optics Communications **117**(5–6), 1995, pp. 417–423.

[5] KRENN J.R., WOLF R., LEITNER A., AUSSENEGG F.R., *Near-field optical imaging the surface plasmon fields of lithographically designed nanostructures*, Optics Communications **137**(1–3), 1997, pp. 46–50.

[6] WEEBER J.-C., KRENN J.R., DEREUX A., LAMPRECHT B., LACROUTE Y., GOUDONNET J.P., *Near-field observation of surface plasmon polariton propagation on thin metal stripes*, Physical Review B **64**(4), 2001, article 045411.

[7] DEVAUX E., EBBESEN T.W., WEEBER J.-C., DEREUX A., *Launching and decoupling surface plasmons via micro-gratings*, Applied Physics Letters **83**(24), 2003, pp. 4936–4938.

[8] WEEBER J.-C., LACROUTE Y., DEREUX A., *Optical near-field distributions of surface plasmon waveguide modes*, Physical Review B **68**(11), 2003, article 115401.

[9] LIU Z., STEELE J.M., SRITURAVANICH W., PIKUS Y., SUN C., ZHANG X., *Focusing surface plasmons with a plasmonic lens*, Nano Letters **5**(9), 2005, pp. 1726–1729.

[10] SALAS-MONTIEL R., APUZZO A., DELACOUR C., SEDAGHAT Z., BRUYANT A., GROSSE P., CHELNOKOV A., LERONDEL G., BLAIZE S., *Quantitative analysis and near-field observation of strong coupling between plasmonic nanogap and silicon waveguides*, Applied Physics Letters **100**(23), 2012, article 231109.

[11] ZHOU L., GAN Q., BARTOLI F.J., DIEROLF V., *Direct near-field optical imaging of UV bowtie nanoantennas*, Optics Express **17**(22), 2009, pp. 20301–20306.

[12] KIM H.W., LEE K.G., KIM D.S., AHN K.J., *Dual mode near-field scanning optical microscopy for near-field imaging of surface plasmon polariton*, Optics Communications **282**(12), 2009, pp. 2442–2445.

[13] RANG M., JONES A.C., ZHOU F., LI Z.-Y., WILEY B.J., XIA Y., RASCHKE M.B., *Optical near-field mapping of plasmonic nanoprisms*, Nano Letters **8**(10), 2008, pp. 3357–3363.

[14] KUBO A., ONDA K., PETEK H., SUN Z., JUNG Y.S., KIM H.K., *Femtosecond imaging of surface plasmon dynamics in a nanostructured silver film*, Nano Letters **5**(6), 2005, pp. 1123–1127.

[15] FUJIKAWA Y., SAKURAI T., TROMP R.M., *Surface plasmon microscopy using an energy-filtered low energy electron microscope*, Physical Review Letters **100**(12), 2008, article 126803.

[16] DOUILLARD L., CHARRA F., KORCZAK Z., BACHELOT R., KOSTCHEEV S., LERONDEL G., ADAM P.-M., ROYER P., *Short range plasmon resonators probed by photoemission electron microscopy*, Nano Letters **8**(3), 2008, pp. 935–940.

[17] HECHT B., BIELEFELDT H., INOUYE Y., POHL D.W., NOVOTNY L., *Facts and artifacts in near-field optical microscopy*, Journal of Applied Physics **81**(6), 1997, pp. 2492–2498.

[18] HATANO H., KAWATA S., *Applicability of deconvolution and nonlinear optimization for reconstructing optical images from near-field optical microscope images*, Journal of Microscopy **194**(2–3), 1999, pp. 230–234.

[19] SUN Z., ZENG D., *Coupling of surface plasmon waves in metal/dielectric gap waveguides and single interface waveguides*, Journal of the Optical Society of America B **24**(11), 2007, pp. 2883–2887.

[20] SUN Z., ZUO X., *Tuning resonant optical transmission of metallic nanoslit arrays with embedded microcavities*, Optics Letters **34**(9), 2009, pp. 1411–1413.

Received January 18, 2013